ORIGINAL ARTICLE

Metal natural product complex Ru-procyanidins with quadruple enzymatic activity combat infections from drug-resistant bacteria

Jie Shan[a,b,†], Xu Jin[a,b,†], Cong Zhang[c,†], Muchen Huang[d,†],
Jianghao Xing[e], Qingrong Li[b], Yuyu Cui[a], Qiang Niu[d],
Xu Lin Chen[a,*], Xianwen Wang[b,f,*]

[a]*Department of Burns, the First Affiliated Hospital of Anhui Medical University, Hefei 230022, China*
[b]*School of Biomedical Engineering, Research and Engineering Center of Biomedical Materials, Anhui Provincial Institute of Translational Medicine, Anhui Medical University, Hefei 230032, China*
[c]*Division of Gastroenterology, the First Affiliated Hospital of USTC, Division of Life Science and Medicine, University of Science and Technology of China, Hefei, Anhui 230026, China*
[d]*The Second Clinical Medical College, Anhui Medical University, Hefei 230022, China*
[e]*Department of Oncology, the First Affiliated Hospital of Anhui Medical University, Hefei 230022, China*
[f]*College and Hospital of Stomatology, Anhui Medical University, Key Lab. of Oral Diseases Research of Anhui Province, Hefei 230032, China*

Abstract Bacterial infection hampers wound repair by impeding the healing process. Concurrently, inflammation at the wound site triggers the production of reactive oxygen species (ROS), causing oxidative stress and damage to proteins and cells. This can lead to chronic wounds, posing severe risks. Therefore, eliminating bacterial infection and reducing ROS levels are crucial for effective wound healing. Nanozymes, possessing enzyme-like catalytic activity, can convert endogenous substances into highly toxic substances, such as ROS, to combat bacteria and biofilms without inducing drug resistance. However, the current nanozyme model with single enzyme activity falls short of meeting the complex requirements of antimicrobial therapy. Thus, developing nanozymes with multiple enzymatic activities is essential. Herein, we engineered a novel metalloenzyme called Ru-procyanidin nanoparticles (Ru-PC NPs) with diverse enzymatic activities to aid wound healing and combat bacterial infections. Under acidic conditions, due to their glutathione (GSH) depletion and peroxidase

---

*Corresponding authors.

E-mail addresses: okcxl@126.com (Xu Lin Chen), xianwenwang@ahmu.edu.cn (Xianwen Wang).

[†]These authors made equal contributions to this work.

(POD)-like activity, Ru-PC NPs combined with H_2O_2 exhibit excellent antibacterial effects. However, in a neutral environment, the Ru-PC NPs, with catalase (CAT) activity, decompose H_2O_2 to O_2, alleviating hypoxia and ensuring a sufficient oxygen supply. Furthermore, Ru-PC NPs possess exceptional antioxidant capacity through their superior superoxide dismutase (SOD) enzyme activity, effectively scavenging excess ROS and reactive nitrogen species (RNS) in a neutral environment. This maintains the balance of the antioxidant system and prevents inflammation. Ru-PC NPs also promote the polarization of macrophages from M1 to M2, facilitating wound healing. More importantly, Ru-PC NPs show good biosafety with negligible toxicity. *In vivo* wound infection models have confirmed the efficacy of Ru-PC NPs in inhibiting bacterial infection and promoting wound healing. The focus of this work highlights the quadruple enzymatic activity of Ru-PC NPs and its potential to reduce inflammation and promote bacteria-infected wound healing.

1. Introduction

Bacterial infections are a major cause of death among humans. Infectious disorders caused by bacteria are often treated with conventional antibiotics, which can be made from natural substances or modified chemicals[1−4]. These antibiotics can disrupt cell membrane/wall formation, protein synthesis, or DNA replication/repair, leading to the death of pathogenic bacteria or inhibition of their growth[5]. Prolonged or unregulated use of antibiotics has given rise to multidrug-resistant superbugs, which pose a significant threat to public health and the environment[6]. By 2050, it is anticipated that drug-resistant bacteria will be the cause of approximately 700,000 annual fatalities, with a total estimated death toll of 10 million[7]. Moreover, conventional antibiotics are often ineffective against bacteria in biofilms due to the protective extracellular polymers that surround them[8]. Thus, discovering new antimicrobial agents and strategies has become a significant challenge.

Nanozymes are widely utilized in antimicrobial research due to their peroxidase (POD)-like activity, which can produce radicals from hydrogen peroxide (H_2O_2) with high antibacterial activity and minimal toxicity[9−13]. Among these radicals, ·OH can cause oxidative damage to cell walls and membranes, and when used in combination with chemodynamic therapy (CDT), it can show more potent antibacterial effects[14]. However, numerous hurdles remain to be overcome in this field, such as the abnormally elevated levels of glutathione (GSH) found in the bacterial microenvironment, which significantly hampers the efficacy of nanozymes[15]. To tackle these prevailing challenges, the integration of nanozymes with other functionalities offers a promising avenue. Notably, within infectious environments, the enzyme glutathione peroxidase (GSH-Px) demonstrates remarkable efficiency in reducing GSH levels. Therefore, the synergistic utilization of peroxidase (POD) and GSH-Px can effectively enhance the generation of reactive oxygen species (ROS) while concurrently depleting excess GSH[16].

Simultaneously, the wound site is frequently accompanied by an inflammatory response that triggers the generation of ROS, including H_2O_2, hydroxyl radicals (·OH), and superoxide anion radicals ($O_2^{·−}$)[17]. Amounts of ROS levels can induce profound oxidative stress, leading to protein damage and the impairment of normal cellular function, thereby giving rise to chronic wounds that, in severe instances, can be life-threatening[18]. Consequently, it is imperative to eradicate bacterial infection and effectively eliminate ROS to facilitate the process of wound healing. Moreover, macrophages play a crucial role in controlling inflammation through phenotypic switching and the clearance of apoptotic neutrophils. However, macrophages with a proinflammatory phenotype (M1) release an excessive quantity of inflammatory factors, while macrophages with an anti-inflammatory phenotype (M2) do not secrete enough[19]. This imbalance in the immune response results in the continual release of ROS, proteases, and free radicals, causing further tissue damage and hindering critical processes such as angiogenesis, collagen deposition, wound re-epithelialization, and wound healing. Therefore, to effectively promote wound healing, it is crucial to eliminate free radicals and regulate macrophage polarization.

Recent reports have suggested that ruthenium metalloenzymes have POD activity and glutathionase properties, making them applicable in noninvasive antimicrobial treatments[20,21]. However, ruthenium alone was not effective in fighting inflammation caused by infected wounds. In contrast to previous antimicrobial nanomaterials, many of which are limiting and inefficient[22,23], natural product antimicrobials have high potential for application[24]. Natural polyphenol procyanidins (PCs) extracted from plants can act as antioxidant, antibacterial, and anti-inflammatory agents[25−27]. Fe-Cur is a novel class of metallo-liganded natural product nanozymes that exhibit excellent antioxidant properties[28]. Although the anti-inflammatory properties of natural product complexes have been extensively researched, their antibacterial effects are not as well documented. Herein, the present study introduced a novel nanozyme composed of procyanidins coordinated with ruthenium, which exhibited four enzymatic activities (Scheme 1). This nanozyme demonstrated effective antibacterial properties by depleting glutathione (GSH) under acidic conditions, as well as POD-like activity. Under neutral conditions, the cat-like ability to provide oxygen, as well as antioxidant and anti-inflammatory activities, was exhibited by the Ru-PC NPs through scavenging ROS and RNS and the presence of PC. The optimal microenvironment for efficient cell proliferation, angiogenesis, granulation tissue formation, and re-epithelialization was fostered by the Ru-PC NPs, which concurrently addressed infection, oxygen supply, free radical scavenging, macrophage polarization from M1 to M2, and inflammation reduction. Additionally, RNA sequencing (RNA-Seq) results demonstrated that Ru-PC NPs interfered with various metabolic processes in *MRSA* bacteria,
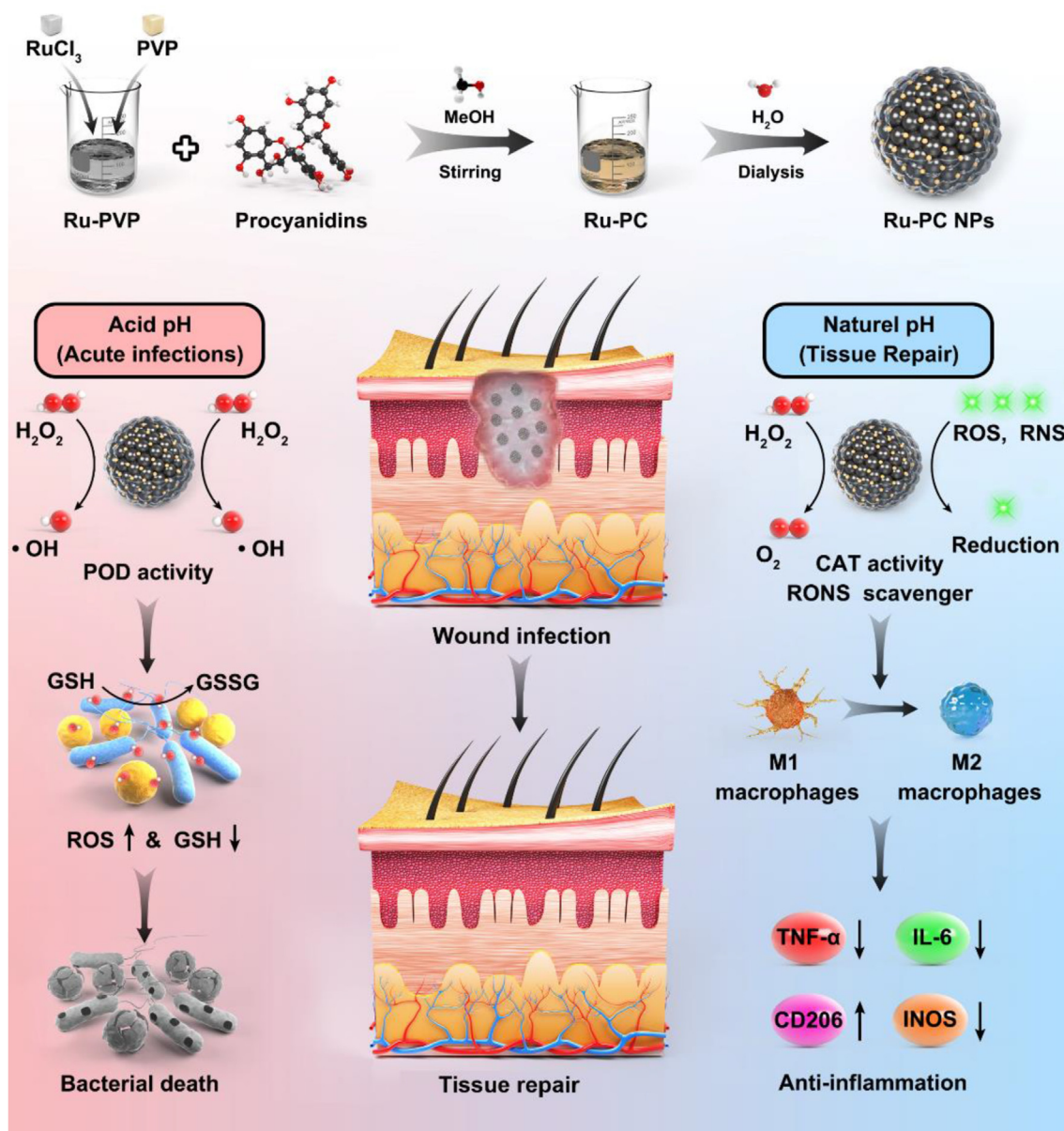
Scheme 1   Schematic illustration of Ru-PC NPs for the treatment of bacterial infection.

including glycolysis, the TCA cycle, pyruvate metabolism, and cysteine synthesis upregulation, thereby exhibiting a potent antibacterial effect. These findings establish the potential of Ru-PC NPs as a highly effective antimicrobial agent capable of replacing antibiotics for treating bacterial-infected wounds.

2.   Materials and methods

2.1.   Materials

RuCl$_3$ (10049-08-8, Shanghai, China) was purchased from Aladdin, and procyanidins (C$_{30}$H$_{26}$O$_{13}$) (4852-22-6, Shanghai, China) and polyvinylpyrrolidone (PVP 9003-39-8, Shanghai, China) were purchased from Macklin. Tryptone soybean broth (LA-0110, China), agar powder (C$_{12}$H$_{18}$O$_9$) (9002-18-0, Beijing, China) were purchased from Solarbio. A bacterial life and death

staining kit (100T) (BB-41-266, Shanghai, China) were purchased from BestBio. Glutathione (CS0260-1 KT, Shanghai, China) (reduced form) was purchased from Aladdin. 5,5′-Dithiobis (2-nitrobenzoic acid) (DTNB) (69-78-3, Chongqing, China), o-phenylenediamine (OPD) (95-54-5, Chongqing, China), 3,3′,5,5′-tetramethylbenzidine (TMB) (54827-17-7, Chongqing, China), diphenyl-2-picrylhydrazyl (DPPH) (1898-66-4, Chongqing, China) and 2,2′-azinobis-(3-ethylbenzthiazoline-6-sulfonate) (ABTS) (30931-67-0, Chongqing, China) were purchased from Macklin.

2.2.   Synthesis of Ru-PC NPs

While preparing a PVP (66 mg) in methanol (5 mL) solution, 20 mg of RuCl$_3$ was gradually added while stirring to 1 mL of methanol. Next, 1 mL of methanol was added dropwise with 10 mg of procyanidin to the solution, which was then agitated for

3 h. Next, the solution was dialyzed against water overnight and collected for subsequent testing.

2.3. Characterization

Transmission electron microscopy (JEM-1400 Plus, Tokyo, Japan) was utilized to investigate the sample morphology, while the chemical composition was determined by X-ray photoelectron spectroscopy (XPS) (Thermo Scientific K-Alpha, Beijing, China). A fluorescence microscope (U-LH100HGAPO, Olympus Corporation, Tokyo, Japan) was employed to capture the fluorescence images. A UV−Vis spectrophotometer (Thermo Scientific Genesys 50, Shanghai, China) was used to measure the UV−Vis absorption spectrum of the substance, and a universal microplate spectrophotometer (Synergy2 SLFPTAD, San Diego, CA, USA) was utilized to determine the optical density (OD).

2.4. Peroxidase-like catalytic activity

The peroxidase-like activity of the material was assessed by mixing it with TMB and OPD reagents, as well as H_2O_2, in an acetate buffer solution with a pH range of 3.0−8.0 at a concentration of 0.12 mol/L. The color reaction at a wavelength of 652 nm for OxTMB and 492 nm for OPD was measured to determine the peroxidase-like activity of the material.

2.5. Detection of catalase-like catalytic activity

Catalase-like catalytic activity was evaluated using a portable dissolved oxygen meter (JPB607A) to measure the oxygen concentration under continuous stirring. Before conducting the experiment, dissolved oxygen was removed from deionized water by purging it with nitrogen for 30 min. The levels of oxygen were measured for various concentrations of Ru-PC NPs and H_2O_2.

2.6. RNS scavenging ability

DPPH and ABTS were selected to evaluate the RNS scavenging ability of the Ru-PC NPs samples mixed with 3 mL of DPPH or ABTS solution and allowed to react in the dark for 20 min. Then, the full wavenumber scanning curves were recorded, and the absorbance values at 517 and 734 nm were measured.

2.7. Evaluation of $O_2^{\cdot-}$ scavenging ability

The ability of Ru-PC NPs to scavenge $O_2^{\cdot-}$ was evaluated using a kit for detecting superoxide anions. The test solution of $O_2^{\cdot-}$ free radicals was prepared as instructed and subsequently exposed to varying concentrations of Ru-PC NP solution at a temperature of 37 °C. After incubation, the solution's absorbance was measured at 550 nm, and the scavenging capacity of Ru-PC NPs against $O_2^{\cdot-}$ was calculated.

2.8. GSH consumption

Ellman's method was employed to detect the consumption of GSH, and all experiments were conducted under dark conditions. By rupturing the disulfide bond (−S−S−), the yellow product 2-nitro-5-thiobenzoic acid was produced when the Ellman reagent 5,5′-dithiobis(2-nitrobenzoic acid) (DTNB) interacted with the mercaptan group (−SH) in glutathione. Ru-PC NPs were coincubated with GSH in PBS for a range of times to examine how GSH consumption varies with time. To assess the amount of GSH depletion, the resultant solution was combined with DTNB and centrifuged, and the residual suspension was subjected to UV−Vis absorption spectroscopy.

2.9. In vitro antibacterial test

The antibacterial performance of Ru-PC NPs was assessed in vitro using the plate counting method to determine the number of CFUs on the plates. Gram-positive and gram-negative bacterial strains, namely, Escherichia coli (E. coli, DH5α) and methicillin-resistant Staphylococcus aureus (MRSA, MU50), were chosen for the experiment. These strains were immersed in an acidic PBS solution with a pH of 5.5. The experiments were divided into two groups: (1) bacteria + Ru-PC NPs and (2) bacteria + Ru-PC NPs + H_2O_2. Concentration gradients of Ru-PC NPs were set at 0, 10, 30, 50, and 80 μg/mL, and the H_2O_2 concentration was maintained at 100 μmol/L in 96-well plates, which were incubated for 6 h. After incubation, 40 μL of the bacterial suspensions were plated onto agar plates and photographed after 6 h to determine the survival rate.

2.10. Live/dead bacterial staining assay

Bacteria incubated with Ru-PC NPs and 100 μmol/L H_2O_2 for 8 h were used for the live/dead bacterial staining assay. The bacterial suspensions were labeled using the Live/Dead BacLight bacterial viability kit, which contained PI and SYTO9. Following different treatments, the bacterial cells were exposed to PI and SYTO9 fluorescence nucleic acid stain and incubated for 25 min in the absence of light. The bacterial cells were then rinsed three times and suspended in 0.9% physiological saline solution. The live and dead cells were observed using a laser scanning microscope.

2.11. Morphological observation of bacteria

The bacteria were fixed with 2.5% glutaraldehyde after 12 h of different treatments. The bacteria were subjected to continuous suspension in ethanol solutions with varying concentrations of 10%, 30%, 50%, 70%, and 90%. After each suspension, the cells were repeatedly suspended in ethanol solutions of the same concentrations and dehydrated for 10 min. In addition, the bacterial samples were dispersed in 200 μL of ethanol, and scanning electron microscopy was used for characterization.

2.12. Cytotoxicity test in vitro

In vitro cytotoxicity assessment of the viability of HUVECs after exposure to Ru-PC NPs at varying concentrations was determined using the CCK-8 kit. Following a 24-h coculture of HUVECs and Ru-PC NPs, the supernatant was discarded, and the cells were washed three times with aseptic buffer. Subsequently, the cells were incubated with 50 μL CCK-8 solution and 450 μL fresh culture medium. The absorbance of the cells was measured at 450 nm using a Thermo Varioskan Flash microplate instrument after 2 h of incubation at 37 °C to quantify cell viability.

2.13.   The assessment of hemolysis

The hemolytic activity assessment involved diluting fresh BALB/c mouse red blood cells with PBS to a 2% concentration. The red blood cell suspension was diluted and combined with different concentrations of Ru-PC NPs solution and then incubated at 37 °C for 4 h. After centrifugation at 2000 rpm for 10 min (H16S0−W, Cence, Changsha, China), the supernatant was collected for analysis. The hemolysis rate of each group was determined by measuring the absorbance of the supernatant at 540 nm using a microporous plate instrument. The hemolysis rate was obtained according to the following Eq. (1):

$$\text{Hemolysis rate } (\%) = \left(A_{\text{sample}} - A_{\text{neg}}\right) / \left(A_{\text{pos}} - A_{\text{neg}}\right) \times 100 \qquad (1)$$

The absorbance of the negative control (A_{neg}) and positive control (A_{pos}) were obtained, and the absorbance of the Ru-PC NPs groups at concentrations of 12.5, 25, 50, 100, and 200 µg/mL were represented by A_{Sample}. The positive and negative controls were ultrasonic water and PBS, respectively.

2.14.   Cell lines and culture conditions

The Chinese Academy of Sciences provided two cell lines: human umbilical vein endothelial cells (HUVECs) and RAW264.7 macrophages. DMEM containing 10% fetal bovine serum (FBS) and supplemented with 1% streptomycin and penicillin was utilized to propagate HUVECs and RAW264.7 cells.

2.15.   ROS staining test

To assess the intracellular scavenging ability of reactive oxygen species by the samples, a DCFH-DA probe was utilized. The cells were plated in 6-well plates and treated with both LPS and samples. After 12 h, the DCFH-DA probe was added and incubated for 20 min, after which fluorescence images were captured for each group.

2.16.   Anti-inflammation assay

All *in vitro* anti-inflammatory assessments were performed using RAW264.7 cells, a mouse macrophage line. To induce macrophage polarization toward the M1 type, LPS solution (100 ng/mL) was added to the culture medium, followed by incubation with 30 and 50 µg/mL Ru-PC NPs to activate the macrophages (500 µL, 2×10^4 cells/mL). After incubation for 24 h, anti-inflammatory activity was evaluated. The distinctive surface biomarkers of M1 and M2 macrophages (INOS and CD206, respectively) were identified using immunofluorescence labeling at various Ru-PC NPs concentrations to measure macrophage polarization. The supernatants were collected, and the concentrations of proinflammatory cytokines (IL-6 and TNF-α) were measured using appropriate enzyme-linked immunosorbent assay (ELISA) quantification kits according to the manufacturer's instructions.

2.17.   In vivo wound healing

Animal experiments were conducted in accordance with the guidelines established by the Institutional Animal Care and Use Committee of Anhui Medical University (approved No. LLSC 20231268). Four groups were formed, consisting of 5 BALB/c mice each, which were randomly divided. The groups were (1) PBS group (control); (2) H_2O_2 group; (3) Ru-PC NPs group; and (4) Ru-PC NPs + H_2O_2 group. Anesthesia was induced in the mice with sodium pentobarbital, and their back hair was shaved. A sterile scalpel was used to create a circular wound with a diameter of 1 cm on the skin. Next, 50 µL of a suspension of *MRSA* (1×10^9 CFU/mL) was applied to the wound and allowed to air dry, and the mice were left for 6 h. Afterward, the wound sites were treated with drops of Ru-PC NPs (100 µg/mL, suspended in PBS) and H_2O_2 (100 µmol/L, suspended in PBS). The size of the mouse skin wound was measured and recorded on Days 1, 4, and 8 after each treatment, and the wound area was calculated using ImageJ software. On Day 8, skin samples from the mice were collected for histopathological examination using HE and Masson staining. Finally, biosafety experiments were conducted by extracting blood and vital organs from the mice.

2.18.   Transcriptome sequencing of MRSA treated with Ru-PC NPs

To investigate the effect of Ru-PC NPs treatment on *MRSA*, transcriptome sequencing was performed on *MRSA* exposed to 50 µg/mL Ru-PC NPs and 100 µmol H_2O_2 for 8 h. TSB medium-treated *MRSA* was used as a control. All samples were processed using an RNA-seq pipeline by Shanghai Personal Biotechnology Co., Ltd. (Shanghai, China). The differentially expressed genes were analyzed using the Kyoto Encyclopedia of Genes and Genomes (KEGG) Mapper, and heatmaps were generated using GraphPad Prism 8.

2.19.   Statistical analysis

The experiments were conducted at least twice or in triplicate. The findings presented in this report are representative. The mean $\pm$ standard deviation (SD) was used to express the quantitative data. One-way analysis of variance (ANOVA) was applied to assess the differences between groups, and statistical significance was deemed present when the *P* value was less than 0.05.

3.   Results and discussion

3.1.   Preparation and characterization of Ru-PC NPs

Ru-PC NPs were synthesized through the dropwise addition of procyanidin to a mixture of RuCl₃ and methanol-dispersed PVP[29]. The presence of PVP facilitated the formation of Ru-PC NPs, which exhibited better water dispersibility (Fig. 1A). TEM analysis was used to characterize the morphology and elemental distribution of the Ru-PC NPs, and the particle size statistics revealed a homogeneous distribution of Ru, C, N, and O elements due to copolymerization (Fig. 1B−F). The prepared Ru-PC NPs also exhibited homogeneity and possessed a small particle size, with an average size of 25 ± 10 nm (Fig. 1G). We conducted measurements on the particle size of Ru-PC NPs and additionally incorporated the zeta potential of the Ru-PC NPs to substantiate the stability of the Ru-PC NPs. The results showed that Ru-PC NPs have a regular particle size distribution and stability in solution (Supporting Information Figs. S1 and S2). The composition, properties, and valence states of the Ru-PC NPs samples were determined using XPS. Ru, C, N and O can be identified in the
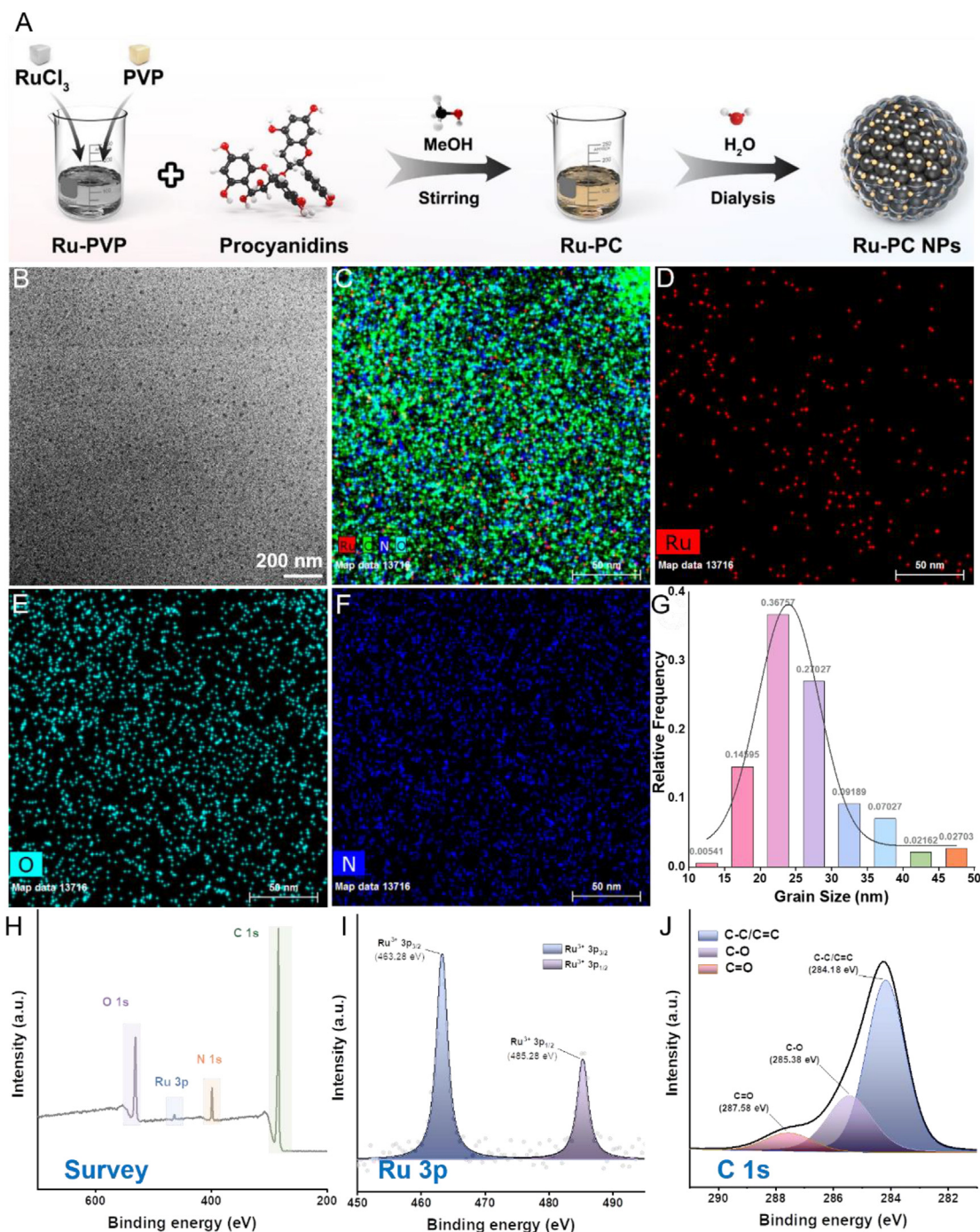
Figure 1 Synthesis and characterization of Ru-PC NPs. (A) Preparation process of Ru-PC NPs. Scale bar = 200 nm. (B−F) TEM mapping of Ru-PC NPs, showing the main elements in nanoparticles. Scale bar = 50 nm. (G) Particle size distribution statistics of Ru-PC NPs. XPS spectra of the (H) survey, (I) Ru 3p region, and (J) C1s region of Ru-PC NPs.

XPS spectrum of the Ru-PC NPs sample (Fig. 1H). Strong binding energy peaks for Ru^{3+} $3p_{3/2}$ and Ru^{3+} $3p_{1/2}$ were observed at 463.28 and 485.28 eV, respectively (Fig. 1I). The fine spectra of C1s show the existence of carbon−carbon single bonds, carbon−oxygen single bonds, carbon−carbon double bonds, and carbon−oxygen double bond structures in Ru-PC NPs (Fig. 1J). The Fourier-transform infrared spectra of Ru-PC NPs also indicate that successful coordination has been achieved between Ru^{3+} and

procyanidins (Supporting Information Fig. S3). These results confirmed the association of Ru with procyanidin in the prepared nanoparticles.

3.2. Multiple enzyme activities of Ru-PC NPs

Ruthenium-based materials are widely used in industrial production due to their various catalytic enzyme-related activities[30]. The

multiple enzyme activity of Ru-PC NPs was evaluated in this study to gain a deeper understanding of their potential applications in the biomedical field (Fig. 2A).

The POD enzyme activity of Ru-PC NPs was assessed by using two chromogenic substrates, OPD and TMB. It was observed that the reaction of H_2O_2 with TMB catalyzed by Ru-PC NPs resulted in a significant increase in absorbance at 652 nm and a darker color compared to TMB with Ru-PC NPs alone. The data showed a positive correlation between the material concentration and peak absorption (Fig. 2B–D). A significant positive relationship was observed between the concentration of Ru-PC NPs and peak absorption in the experiments concerning OPD, indicating that the concentration of Ru-PC NPs had an impact on peak absorption (Fig. 2E–G), thus indicating the POD enzyme-related activity of Ru-PC NPs[31]. The catalytic activities of the POD-like characteristics of Ru-PC NPs were contingent upon the pH value of the solution. A superior catalytic performance of Ru-PC NPs was observed as the pH of the solution decreased (Supporting Information Fig. S4).

Furthermore, Ru-based materials are known to have good glutathione depletion capacity. The GSH-Px-like nanase activity of Ru-PC NPs was investigated through the use of DTNB as a probe, as demonstrated in this study. After incubation of Ru-PC NPs at a concentration of 50 μg/mL for 5 h, GSH was completely depleted (Fig. 2H), indicating the good GSH depletion capacity of Ru-PC NPs.

Notably, a substantial amount of oxygen was generated from H_2O_2 in the presence of Ru-PC NPs, indicating the existence of catalase (CAT) enzyme activity in Ru-PC NPs (Fig. 2I)[32]. Under neutral conditions, the CAT activity of Ru-PC NPs was higher than that under acidic conditions (Supporting Information Fig. S5).

To verify the capacity of Ru-PC NPs to neutralize oxygen radicals, a WST-1 assay was performed to assess their ability to quench $O_2^{\cdot-}$. The results revealed that Ru-PC NPs possessed potent superoxide dismutase (SOD) activity (Fig. 2J)[33].

Moreover, Ru-PC NPs exhibited excellent antioxidant capacity by eliminating free radicals under neutral conditions. The radical scavenging ability of Ru-PC NPs was assessed by utilizing DPPH and ABTS as model molecules. With the increase in the concentration of Ru-PC NPs, the solution exhibited a decrease in color intensity, and its absorption peak at the corresponding wavelength decreased, demonstrating the radical scavenging ability of Ru-PC NPs (Fig. 2K and L). An increase in the concentration of Ru-PC NPs resulted in an increase in the scavenging ratios of DPPH and ABTS, as observed in our experiments (Fig. 2M). It can be inferred from these findings that a substantial antioxidation capability is exhibited by Ru-PC NPs, which is expected to facilitate skin regeneration by diminishing ROS and RNS at the wound site under neutral conditions[34]. Ru-PC NPs possess multiple enzymatic activities, including POD, GSH-Px-like nanase, SOD, and CAT enzyme activities, as well as excellent antioxidation capacity. These findings suggest that Ru-PC NPs hold great potential for antibacterial and anti-inflammatory activities, making them promising candidates for biomedical applications.

3.3. *In vitro antibacterial efficiency assessment*

The outstanding POD-like and GSH-Px-like activities of Ru-PC NPs prompted the investigation of their potential antibacterial properties through *in vitro* experiments. Although H_2O_2 is commonly used for bacterial treatment, its low inherent content in bacteria limits its antibacterial efficacy. In contrast, ·OH radicals are highly toxic oxidants that can cause damage to various biological macromolecules, resulting in bacterial death[35]. The catalytic activity of Ru-PC NPs, similar to that of POD, enables the decomposition of low concentrations of H_2O_2, resulting in the generation of highly toxic ·OH, which enhances the antimicrobial effectiveness. The addition of H_2O_2 to Ru-PC NPs resulted in a further decrease in the *E. coli* and *MRSA* survival rates (Fig. 3A and C). By means of statistical analysis, it was demonstrated that there is a direct correlation between the concentration of Ru-PC NPs and their antibacterial performance, and the synergistic effect of the combination of Ru-PC NPs with H_2O_2 notably enhanced their antibacterial efficacy (Fig. 3B and D). When compared to the traditional antibiotic vancomycin, Ru-PC NPs + H_2O_2 exhibit superior antibacterial activity (Supporting Information Fig. S6). Additional evidence for the potent antibacterial activity of Ru-PC NPs was provided by the live/dead assay. To directly determine the viability of bacteria, they were stained with propidium iodide (PI, red fluorescence) and SYTO9 (green fluorescence) after treatment with different agents (Fig. 3E and F). Consistent with previous results, Ru-PC NPs alone showed only weak antibacterial effects, but their combination with H_2O_2 significantly enhanced their bactericidal effects. This suggests that Ru-PC NPs can effectively kill bacteria by catalyzing the production of ·OH radicals by H_2O_2, owing to their similar OXD and POD activities.

To investigate the bactericidal mechanism of Ru-PC NPs, the morphology and ROS content of bacteria were studied after treatment with different agents. SEM analysis showed that Ru-PC NPs induced significant morphological alterations in the bacterial cells. The bacterial cell membrane was disrupted in the Ru-PC NPs + H_2O_2 group, leading to the collapse and wrinkling of the bacterial surface. Damage to the bacterial membranes was further analyzed using SEM images. For *E. coli*, the bacterial membrane was lysed and ruptured, while the edges of the bacterial membrane became blurred for *MRSA* in the Ru-PC NPs + H_2O_2 group, indicating the loss of some intracellular matrix (Fig. 4A and B). For the healing of wounds induced by drug-resistant bacteria, the disruption of bacterial membrane formation and its protection against wound healing is of paramount importance. Hence, further investigation was undertaken to examine the bactericidal effect of Ru-PC NPs + H_2O_2 on bacterial biofilms. As illustrated in the Supporting Information Figs. S7 and S8, a pronounced disruptive effect on biofilms was observed with Ru-PC NPs + H_2O_2.

In addition, the production of bacterial ROS was evaluated using DCFH-DA (Fig. 4C). Based on these findings, a possible bactericidal mechanism of Ru-PC NPs was proposed. First, Ru-PC NPs exhibited OXD-like catalytic activity, which converted O_2 to ROS, leading to the death of bacteria. Second, Ru-PC NPs demonstrated POD-like activity, catalyzing the production of large amounts of ·OH from low concentrations of H_2O_2, causing damage to the bacterial cell membrane and cell wall. Third, Ru-PC NPs possessed GSH-Px activity, depleting GSH in bacteria and thereby enhancing the antibacterial effect of the catalytic treatment (Fig. 4D).

3.4. *In vitro anti-inflammation assays*

The biocompatibility of the prepared Ru-PC NPs was initially assessed using HUVECs and RAW264.7 cells. After coculture with Ru-PC NPs for 24 h, the cell viability assay of these cells
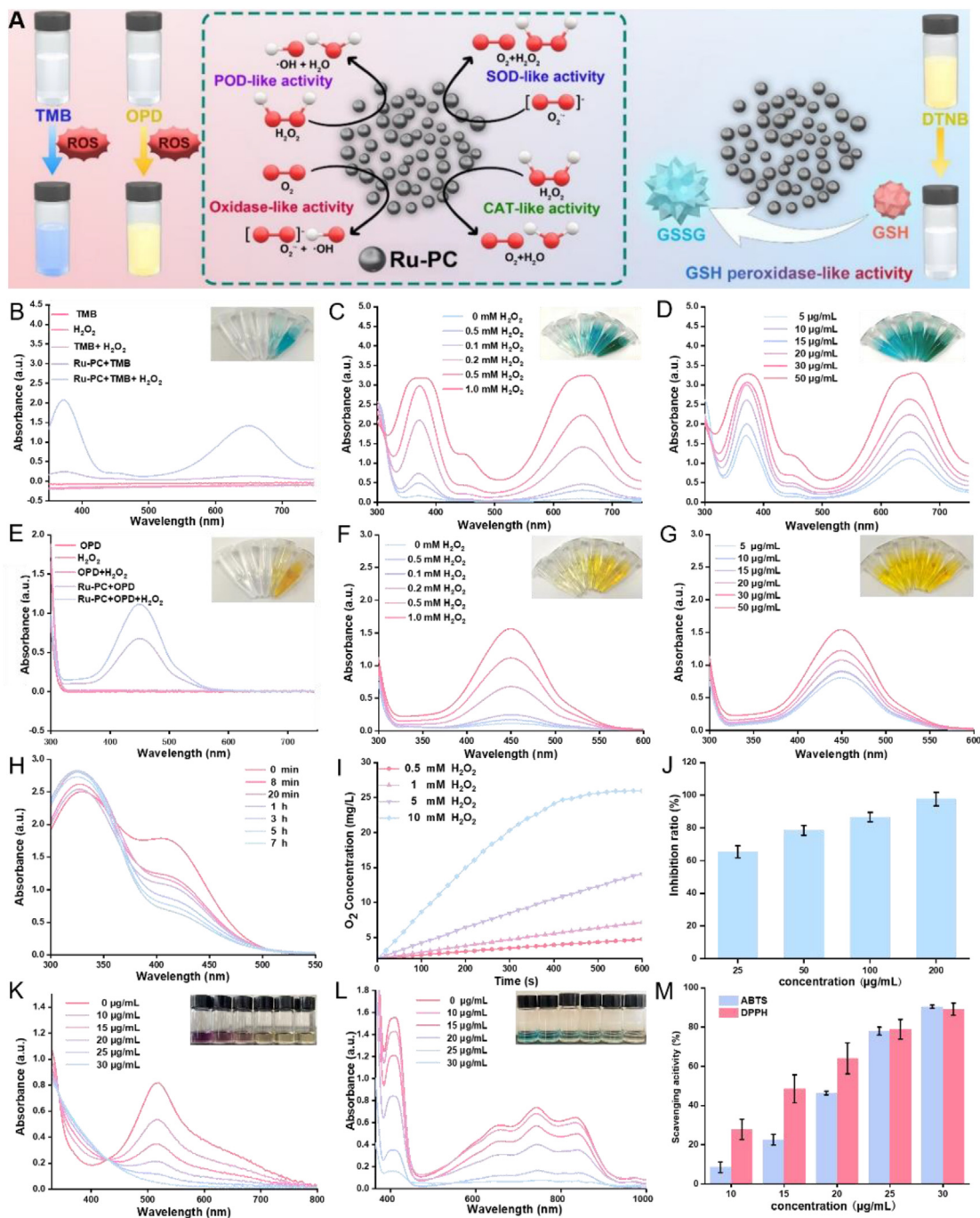
Figure 2 Properties of Ru-PC NPs. (A) Schematic diagram of Ru-PC NPs with SOD-like, OXD-like, POD-like, CAT-like and GSH-Px-like activities. (B) UV−Vis spectra of solutions including TMB alone, H_2O_2, TMB + H_2O_2, Ru-PC NPs + OPD, and Ru-PC NPs + TMB + H_2O_2 after 0.5 h of reaction. (C) OXD-like activity. (D) POD-like activity of Ru-PC NPs using a TMB probe. (E) UV−Vis spectra of solutions including OPD alone, H_2O_2, TMB + H_2O_2, Ru-PC NPs + TMB, and Ru-PC NPs + TMB + H_2O_2 after 0.5 h of reaction. (F) OXD-like activity. (G) POD-like activity of Ru-PC NPs using an OPD probe. (H) Time-dependent GSH depletion of Ru-PC NPs with a DTNB probe at a concentration of 50 μg/mL (I) CAT-like activity with different concentrations of Ru-PC NPs. (J) SOD-like activity with different concentrations of Ru-PC NPs using a SOD kit. (K) DPPH scavenging effect of Ru-PC NPs. (L) ABTS scavenging effect of Ru-PC NPs. (M) DPPH and ABTS scavenging ratio of Ru-PC NPs. Data are presented as mean ± SD, $n = 3$.

showed that the cytocompatibility was excellent (Fig. 5A and B). Additionally, hemolysis assays showed that these hydrogels had good hematological biocompatibility, with hemolysis rates <5% (Fig. 5C). An *in vitro* angiogenesis experiment was conducted to assess the potential impact of Ru-PC NPs on

angiogenesis. Increased loop formations and connections were observed in HUVECs treated with Ru-PC NPs compared to the control group (Supporting Information Fig. S9). Thus, these results confirmed the biocompatibility of the synthesized Ru-PC NPs.
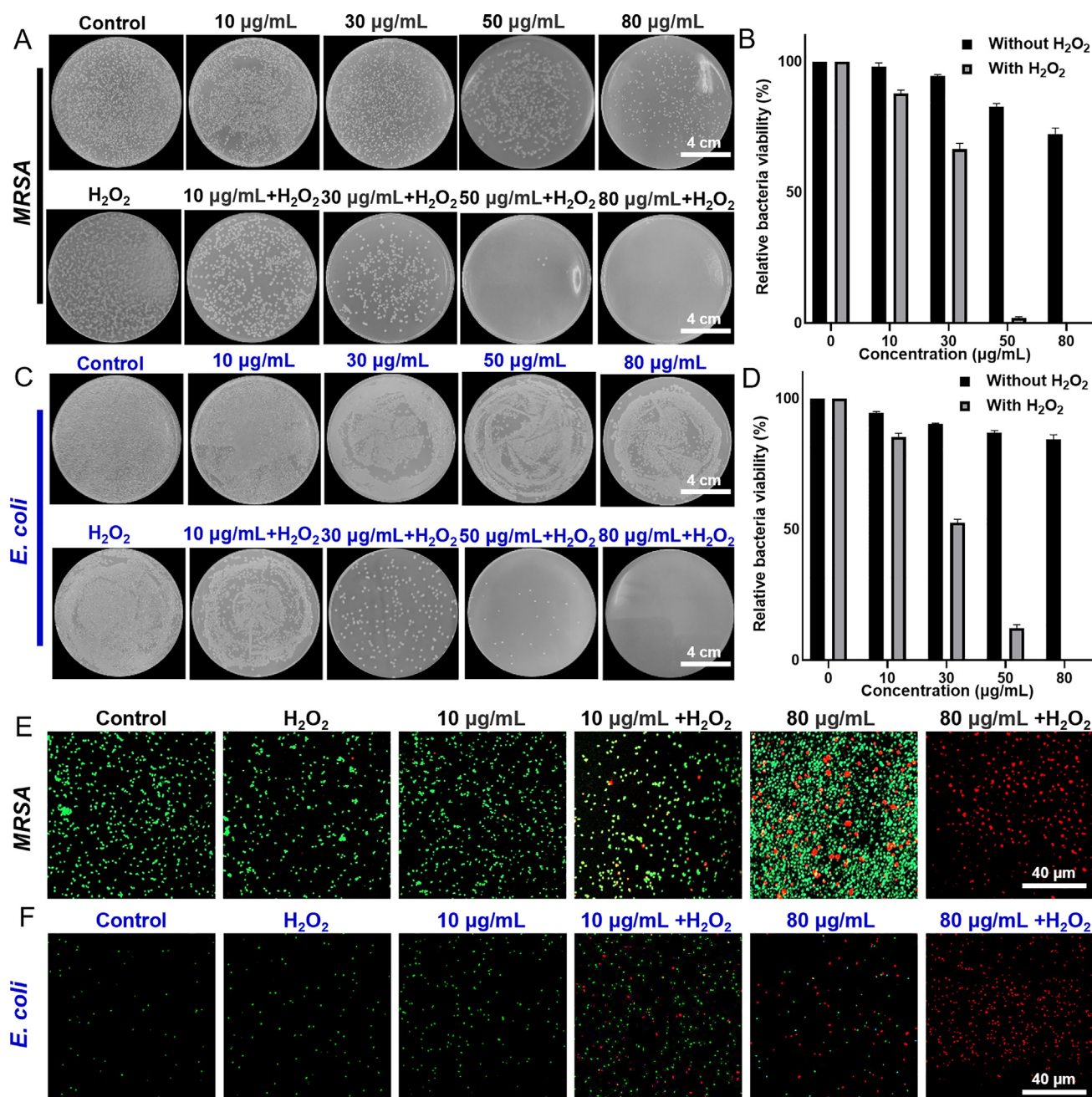
Figure 3 *In vitro* antibacterial performance of Ru-PC NPs (concentration μg/mL). (A) Photographs of bacterial colonies and (B) relative bacterial viability of *MRSA* under different conditions. (C) Photographs of bacterial colonies and (D) relative bacterial viability of *E. coli* after different treatments. Typical fluorescence images of dead (red) and live (green) bacteria after various treatments: (E) *MRSA*; (F) *E. coli*. Data are presented as mean ± SD, n = 3.

To assess the extracellular oxidative protection of RAW264.7 cells against LPS-induced ROS in the presence of various concentrations of Ru-PC NPs, intracellular ROS levels were measured by DCFH-DA staining. In the absence of stimulation, the blank group showed almost no green fluorescence, and the fluorescence intensity (FL) was extremely low. After stimulation by LPS, stronger green fluorescence and a new peak in the FL distribution map were observed in the control cells, indicating exposure to oxidative stress. However, cells protected by low and

high Ru-PC NPs displayed weaker fluorescence, with an FL distribution plot similar to that of the blank group (Fig. 5D). Additionally, the corresponding flow cytometry results confirmed this finding (Fig. 5G and H). This indicates that the addition of Ru-PC NPs had a superior protective effect on LPS and better scavenging of ROS with increasing Ru-PC NPs concentrations.

The chemokine cytokine IL-6 is known to play a role in the synthesis of acute phase proteins and contributes to the inflammatory response. TNF-α, a key proinflammatory cytokine, also
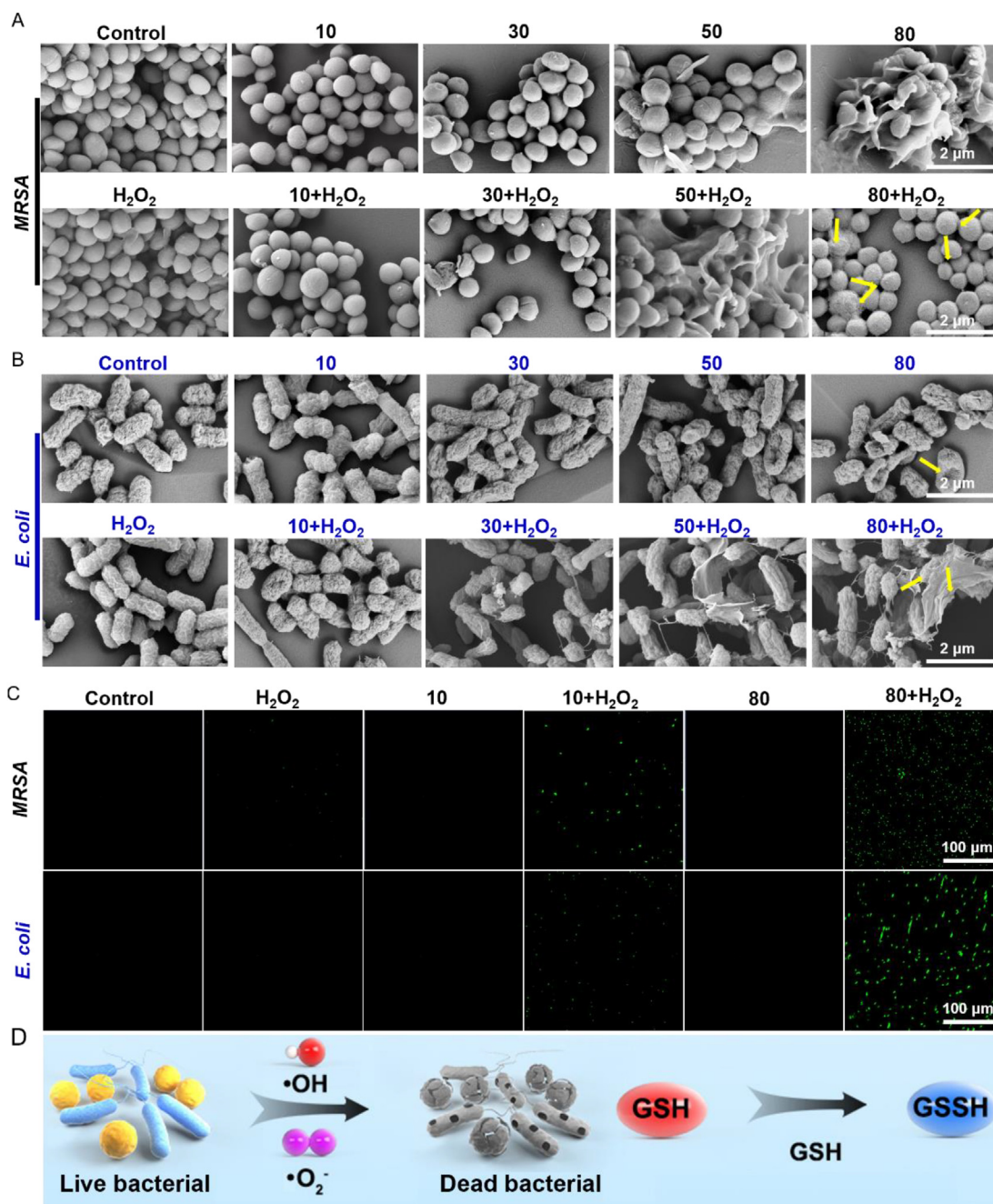
Figure 4 Antibacterial mechanism of Ru-PC NPs. (A) Typical SEM images of *MRSA* after various treatments. (B) Typical SEM images of *E. coli*. after various treatments. Typical fluorescence images of (C) *E. coli* and *MRSA* using a DCFH-DA probe after various treatments. (D) The possible mechanism of Ru-PC NPs for high-efficiency antibacterial activity *in vitro*.

promotes the involvement of T cells in the inflammatory signaling cascade[36]. The levels of these cytokines were evaluated using immunofluorescence, and the results showed that the low Ru-PC NPs and high Ru-PC NPs groups had significantly lower levels of IL-6 and TNF-α than the LPS group (Fig. 5E and F). Both fluorescence intensity statistics and ELISA results confirmed that the concentrations of IL-6 and TNF-α were decreased in the groups treated with low and high concentrations of Ru-PC NPs (Fig. 5I−L).

The strong anti-inflammatory properties of this nanozyme may be attributed to its potent ability to scavenge ROS and function as a powerful antioxidant, which can ultimately promote M2 macrophage polarization[37]. This is especially important since inflammatory reactions sometimes involve an initial rise in ROS generation that might amplify inflammatory cascade activity[38]. To confirm this, representative markers of M2 macrophages (CD206) and M1 macrophages (iNOS) were further detected in each group using immunofluorescence staining. The
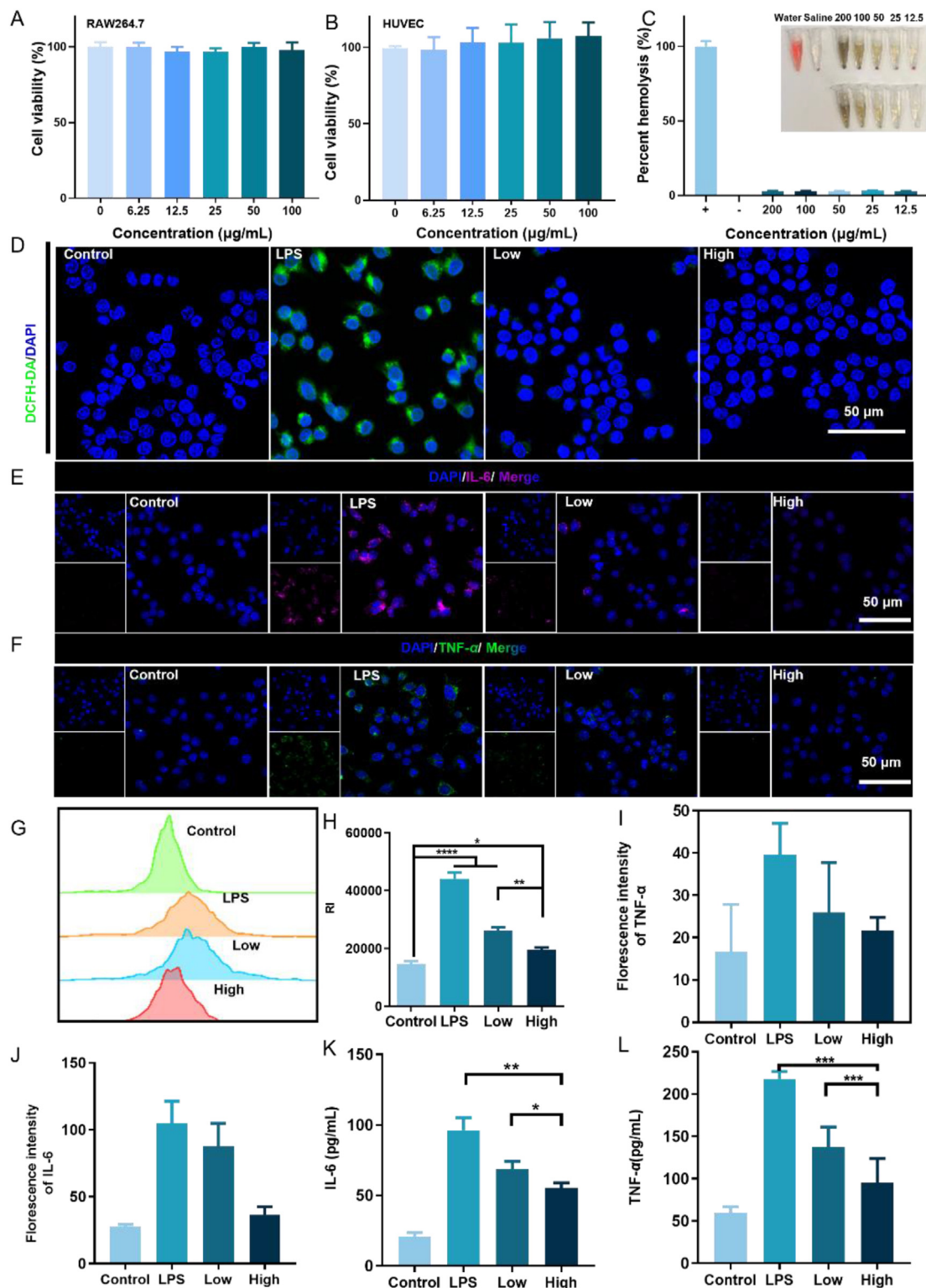
Figure 5 ROS-scavenging and anti-inflammatory ability of Ru-PC NPs (low: 30 μg/mL, high: 50 μg/mL). (A) RAW264.7 cell viability at 24 h. (B) HUVEC viability at 24 h. (C) Hemolysis rate and digital photograph of red blood cells after different treatments. (D) Confocal images of ROS generation in LPS-treated RAW264.7 cells after Ru-PC NP treatment by DCFH-DA staining. (E) Immunofluorescence staining of IL-6. (F) Immunofluorescence staining of TNF-α. (G) Flow cytometry statistics of ROS in each group; (H) ROS fluorescence intensity statistics of each group. (I–J) Fluorescence intensity statistics of IL-6 and TNF-α. (K, L) Proinflammatory cytokines (IL-6 and TNF-α) secreted by primary and LPS-stimulated macrophages. Data are presented as mean ± SD ($n = 3$). *$P < 0.05$; **$P < 0.01$; ***$P < 0.001$; ****$P < 0.0001$, one-way ANOVA.
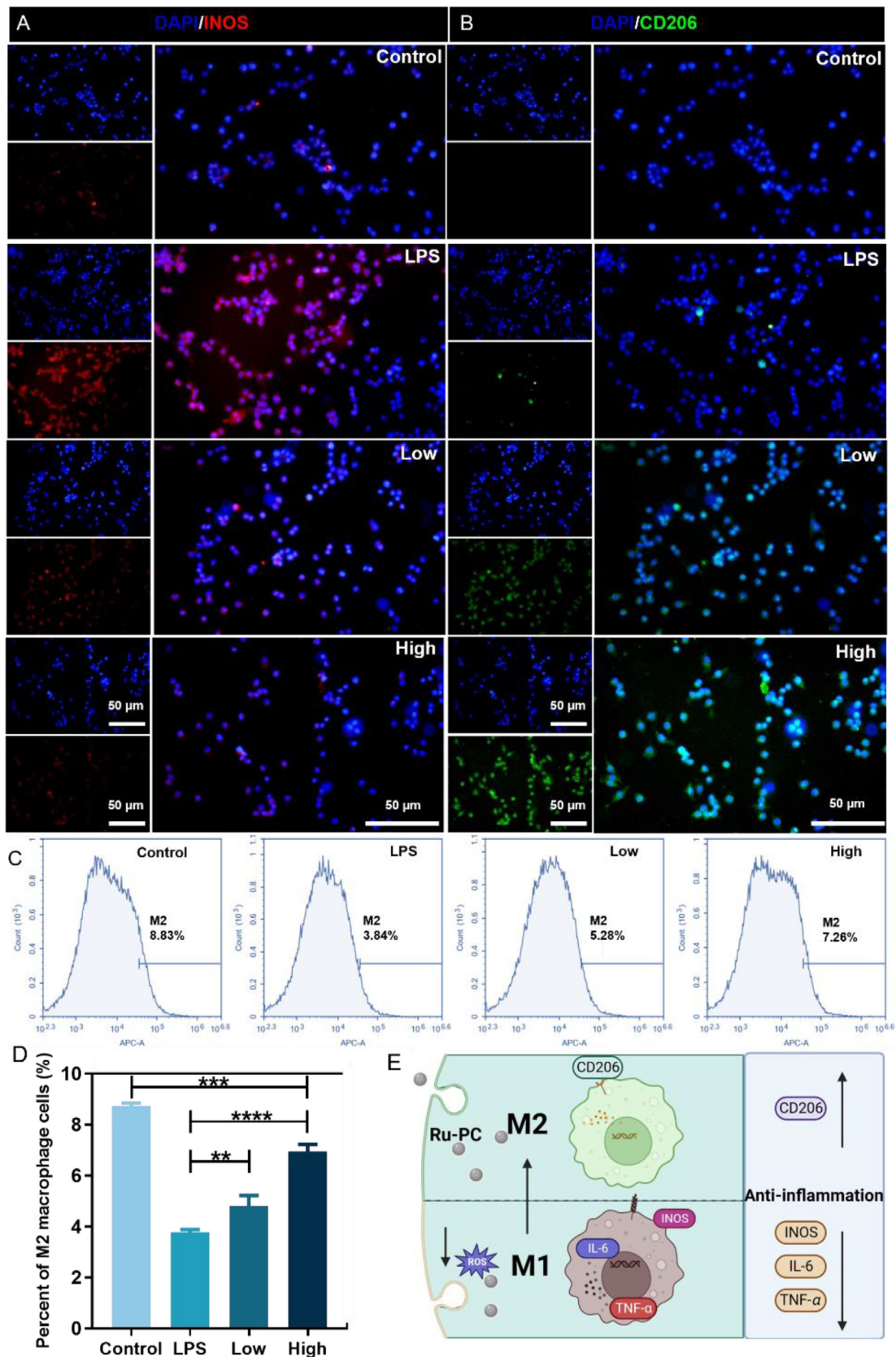
Figure 6 Evaluation of macrophage polarization in RAW264.7 cells. (A, B) Immunofluorescence staining of iNOS (red), CD206 (green), and DAPI (blue) in RAW264.7 cells after coculture with control or Ru-PC NPs for 24 h. (C) Flow cytometry analysis of M2 macrophages. (D) Percent of M2 macrophages according to flow cytometry results. (E) Illustration of Ru-PC NPs modulating macrophage polarization. Data are presented as mean ± SD (*n* = 3). ***P* < 0.01; ****P* < 0.001; *****P* < 0.0001, one-way ANOVA.
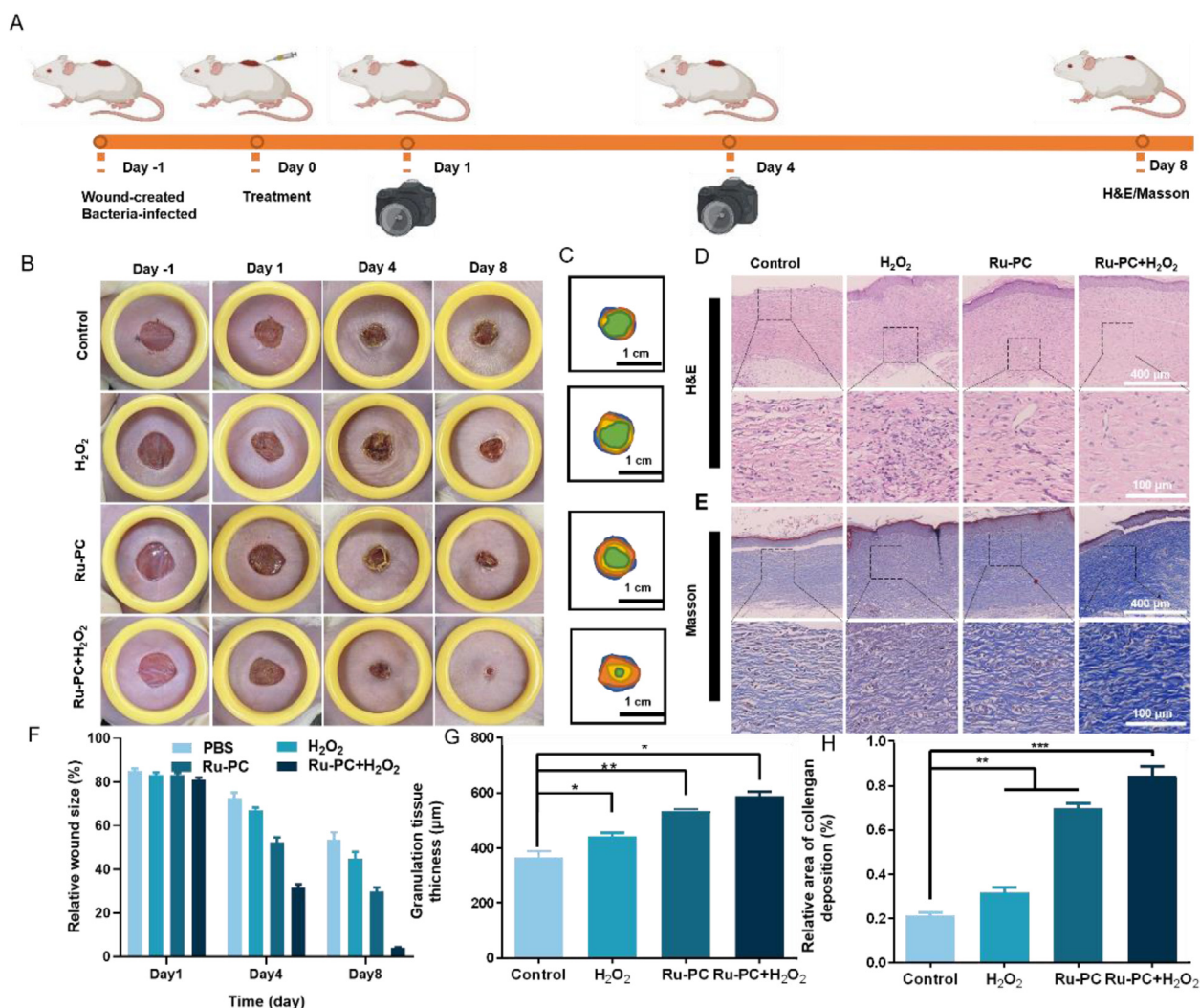
Figure 7 Evaluation of the effect of Ru-PC NPs on *in vivo* infection in animal wounds. (A) Treatment of a *MRSA*-infected wound; (B) Photographs of the wound on Days −1, 1, 4, and 8; (C) Wound closure traces on Days −1, 1, 4, and 8; (D, E) H&E and Masson's staining of the wound on Day 8; (F) Wound area statistics in different groups; (G, H) Relative quantitative analysis of epidermal thickness and collagen deposition. Data are presented as mean ± SD ($n = 4$). *$P < 0.05$; **$P < 0.01$; ***$P < 0.001$; one-way ANOVA.

experimental design utilized macrophages treated with LPS as the positive control group, whereas untreated macrophages were utilized as the negative control group. As shown in Fig. 6A, positive staining for iNOS was more prominent in the LPS-treated group than in the control group, while significantly lower iNOS results were observed in the low and high Ru-PC NPs groups. The concentration-dependent effect was more pronounced as the Ru-PC NPs concentration increased. The results shown in Fig. 6B indicated a significant increase in CD206 levels in the low and high Ru-PC NPs groups. The flow cytometry results provided further evidence that Ru-PC NPs promoted the polarization of M2 macrophages (Fig. 6C and D). The results obtained provided compelling evidence for the anti-inflammatory properties of Ru-PC NPs. As demonstrated in Fig. 6E, the potent antioxidant and ROS scavenging capabilities of Ru-PC NPs led to a superior anti-inflammatory effect, which subsequently led to a decrease in the levels of inflammatory factors such as IL-6 and TNF-α, ultimately inducing macrophage polarization toward the M2 phenotype.

3.5. Biocompatibility of Ru-PC NPs

The *in vivo* toxicity of Ru-PC NPs was assessed, and routine blood analysis of mice treated with Ru-PC NPs demonstrated that the data remained within normal levels (Supporting Information Fig. S12A). H&E staining imaging revealed no significant toxicity in the heart, liver, spleen, lungs, and kidneys of mice treated with Ru-PC NPs (Fig. S12B), indicating that Ru-PC NPs are a safe and effective treatment for bacterially infected wounds.

3.6. In vitro antibacterial and wound healing assays

Given the multiple enzymatic activities and antimicrobial properties described earlier, it is believed that the utilization of Ru-PC NPs can be effective for the treatment of *MRSA*-infected wounds. Wound infection models were created on Day −1 and treated on Day 0, and wound pictures were taken on Days 1, 4, and 8 (Fig. 7A). The results illustrated the effectiveness of Ru-
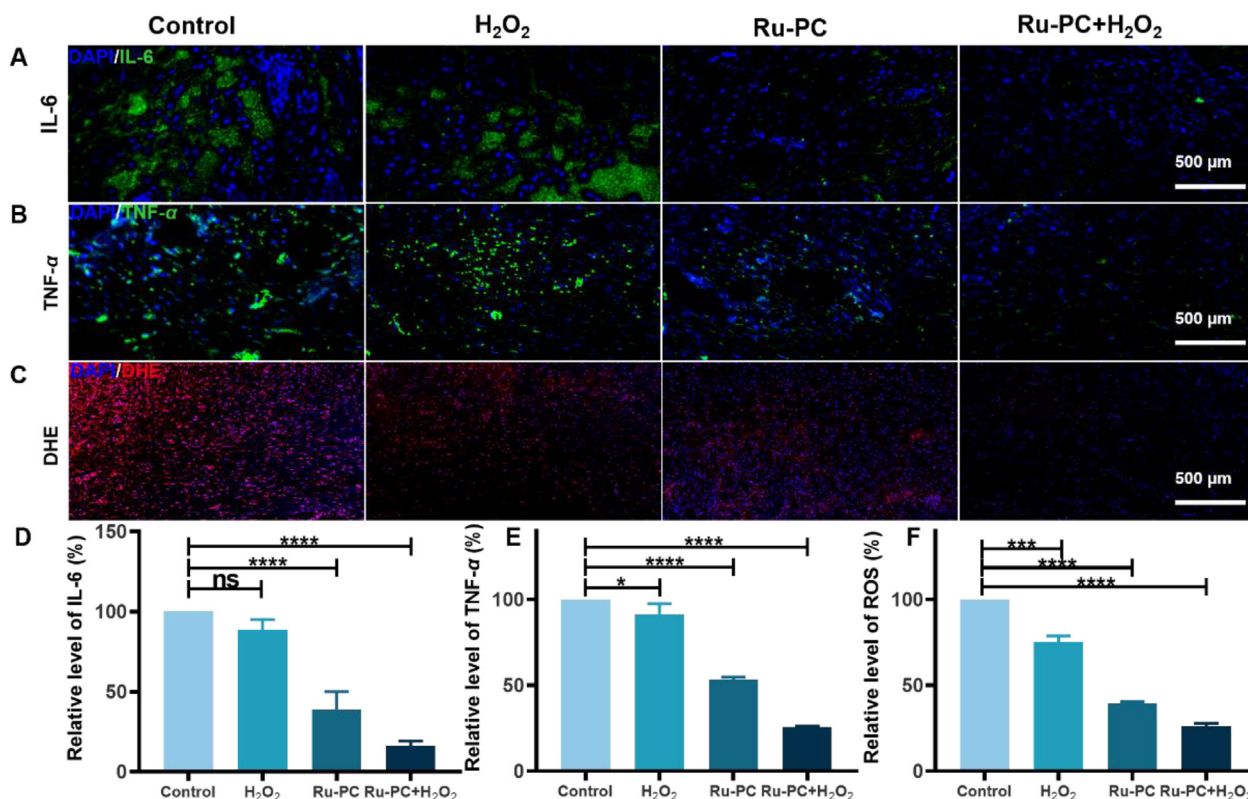
Figure 8 Immunofluorescence staining image of wound tissues. (A−C) Immunofluorescence staining images of IL-6, TNF-α, DHE on Day 8; (D) Statistical analysis of IL-6 levels in wounds ($n = 3$); (E) Statistical analysis of TNF-α levels in wounds ($n = 3$); (F) Statistical analysis of ROS levels in wounds ($n = 3$). Data are presented as mean ± SD ($n = 3$). *$P < 0.05$; ***$P < 0.001$; ****$P < 0.0001$; ns, not significant. One-way ANOVA.

PC NPs in treating infected wounds (Fig. 7B and C). In comparison to the conventional antibiotic vancomycin, a more effective therapeutic outcome and accelerated wound healing rate are achieved with Ru-PC NPs + H_2O_2 in the context of bacterial infections in animal wounds (Supporting Information Figs. S10 and S11). The improved healing in the Ru-PC NPs + H_2O_2 group can be attributed to the heightened GSH-Px and POD-like activities, which resulted in more efficient bacterial eradication. Furthermore, the nanozyme demonstrated a superior antioxidant defense system by exhibiting high CAT-like, SOD-like, and ·OH scavenging abilities. Compared to Day −1, the wound area progressively decreased in all four groups on Days 1, 4, and 8, with the most substantial decrease observed in the Ru-PC NPs + H_2O_2 group (Fig. 7F). Histological analysis using hematoxylin and eosin staining (H&E) was further performed to evaluate wound healing efficiency. The degree of wound healing can be indicated by the thickness of granulation tissue, which forms when the surrounding naïve connective tissue proliferates to replace necrotic parenchymal tissue during tissue injury (Fig. 7D). As shown in Fig. 7G, the thickness of granulation tissue in the Ru-PC NPs + H_2O_2 group was significantly higher than that in the other three groups, indicating better wound healing efficacy. Collagen regeneration on the trauma surface during the transformation of granulation tissue into scar tissue is also an important indicator of tissue remodeling and tensile strength[39]. Masson staining was conducted on

Day 8 to confirm collagen deposition. Fig. 7E shows the stained collagen in blue, and all groups displayed significant areas of epidermal structure defects, with a large number of inflammatory cells observed in the control group. Collagen deposition was significantly higher in the Ru-PC NPs + H_2O_2 group than in the control group (Fig. 7H), indicating that multiple classes of enzyme activity, which catalyze intracellular cascade reactions that resemble intracellular antioxidant defense systems[40], may have promoted collagen deposition in the Ru-PC NPs + H_2O_2 group.

3.7. Immunofluorescence analysis

To assess the inflammatory response, TNF-α and IL-6 immunofluorescence staining was performed. The control group exhibited the highest TNF-α and IL-6 expression levels (Fig. 8A and B), indicating an intense inflammatory response. Furthermore, the relative quantitative analysis (Fig. 8D and E) indicated that the Ru-PC NPs + H_2O_2 group had the lowest TNF-α and IL-6 expression levels, indicating a reduced presence of inflammation or infection.

To investigate the mechanism of ROS scavenging by Ru-PC NPs, the ROS levels in tissues were quantified by employing a DHE probe[41]. The results, as shown in Fig. 8C, indicated that the control group had strong red fluorescence, whereas the Ru-PC NPs + H_2O_2 group had very little red fluorescence, suggesting
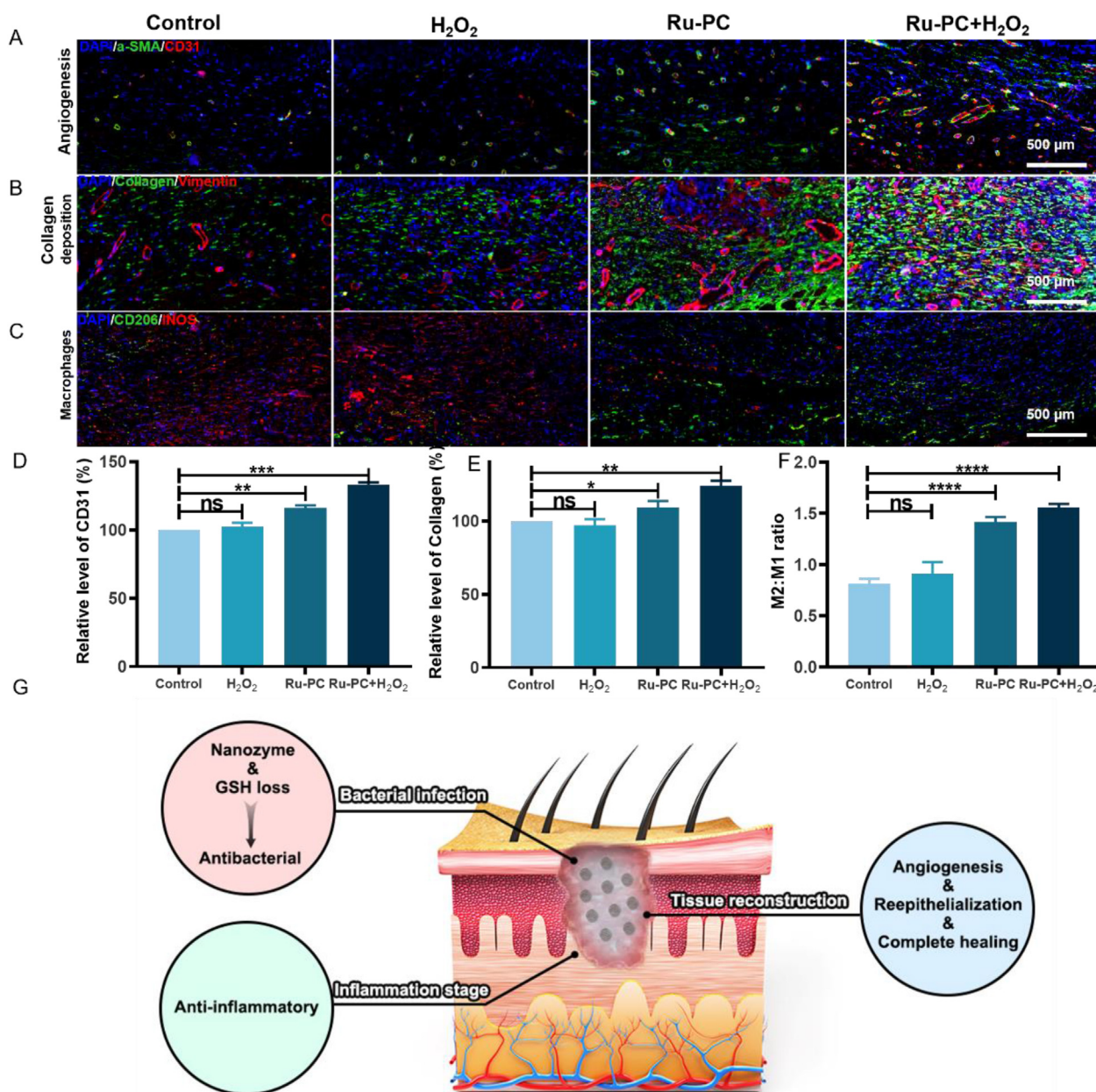
Figure 9 Double immunofluorescence staining study of wound healing. (A) Immunofluorescence staining of CD31 and α-SMA in wounds on Day 8; (B) Immunofluorescence staining of collagen and vimentin in wounds on Day 8; (C) Immunofluorescence staining of CD206/INOS in wounds on Day 8; (D) Quantitative analysis of CD31; (E) Quantitative analysis of collagen; (F) Quantitative analysis of the M1/M2 ratio; (G) Schematic representation of the mechanism of action of Ru-PC NPs in repairing bacterially infected wounds. Data are presented as mean ± SD ($n = 3$). *$P < 0.05$; **$P < 0.01$; ***$P < 0.001$; ****$P < 0.0001$; ns, not significant. one-way ANOVA.

that the nanozyme has the ability to mimic the antioxidant defense system and effectively scavenge ROS, as shown in Fig. 8F.

Accelerating wound healing in bacterial infections can be achieved by promoting epidermal formation, collagen deposition, and neovascularization. Neovascularization, an important indicator of wound healing, was detected through double immunofluorescence staining for α-smooth muscle actin (α-SMA) and CD31[42]. The expression of CD31 was significantly higher in the Ru-PC NPs and Ru-PC NPs + H_2O_2 groups, as shown in Fig. 9A and D, indicating that Ru-PC NPs + H_2O_2 had better pro-

vascularization ability and could promote wound healing more effectively.

Additionally, as demonstrated in Fig. 9B and E, collagen deposition in granulation tissue was assessed using a twofold immunofluorescence staining procedure that included both collagen and waveform proteins, which are fibroblast indicators. The increased deposition of the extracellular matrix (ECM) and directed alignment of collagen fibers are needed for the promotion of ECM construction[43].The least amount of collagen was observed in the control group according to the results, while the Ru-PC

NPs + H$_2$O$_2$ group had higher collagen deposition and a greater degree of oriented alignment, indicating improved collagen growth and favorable wound repair.

During wound healing, macrophages play a crucial role in which M1 macrophages mediate the proinflammatory response and M2 macrophages mediate the anti-inflammatory response. To assess the anti-inflammatory properties of Ru-PC NPs, double immunofluorescence staining was carried out to detect M2 macrophages (CD206) and M1 macrophages (INOS)[44]. The findings demonstrated that there was an elevation in M2 macrophages and a reduction in M1 macrophages in both the Ru-PC NPs and Ru-PC NPs + H$_2$O$_2$ groups (Fig. 9C and F), indicating their superior anti-inflammatory capacity and mitigated inflammatory response. It is worth noting that the Ru-PC NPs + H$_2$O$_2$ group exhibited the most potent anti-inflammatory ability. Therefore, combining Ru-PC NPs with hydrogen peroxide is an optimal therapeutic approach for bacterial wound healing (Fig. 9G).

3.8. Genome analysis of the antibacterial effect of Ru-PC NPs

To clarify the molecular mechanisms responsible for the anti-MRSA activity of Ru-PC NPs, transcriptome sequencing was performed to identify DEGs in MRSA treated with Ru-PC

NPs + H$_2$O$_2$ compared to the control group[45]. In total, 126 DEGs were upregulated, and 182 DEGs were downregulated. Representative DEGs are presented in Fig. 10A and B. In this study, high-throughput sequencing was undertaken to scrutinize the genomic landscape of the Ru-PC NPs + H$_2$O$_2$ group in relation to the H$_2$O$_2$, Ru-PC NPs, and vancomycin groups. The discernment of differentially expressed genes among these groups is deemed crucial for gaining insights into the underlying molecular mechanisms linked to their distinct phenotypic characteristics (Supporting Information Figs. S13−S15). GO enrichment analysis was performed to functionally categorize the DEGs (Supporting Information Fig. S16). Classification and KEGG pathway enrichment analyses revealed that the antibacterial activity of Ru-PC NPs operates through multiple mechanisms (Fig. 10C and D).

First, Ru-PC NPs were found to inhibit the glycolytic pathway of bacteria[46]. Previous studies have identified ALDO and GAPDH as key factors in the antimicrobial mechanism[47]. These genes are regulated by exogenous bacterial toxins such as LPS, which can induce their expression. ALDO and GAPDH are considered regulators of antimicrobial activity in the glycolytic pathway, as they modulate ATP content and the NADH/NAD$^+$ ratio in bacteria, thereby affecting energy metabolism and redox status[48].
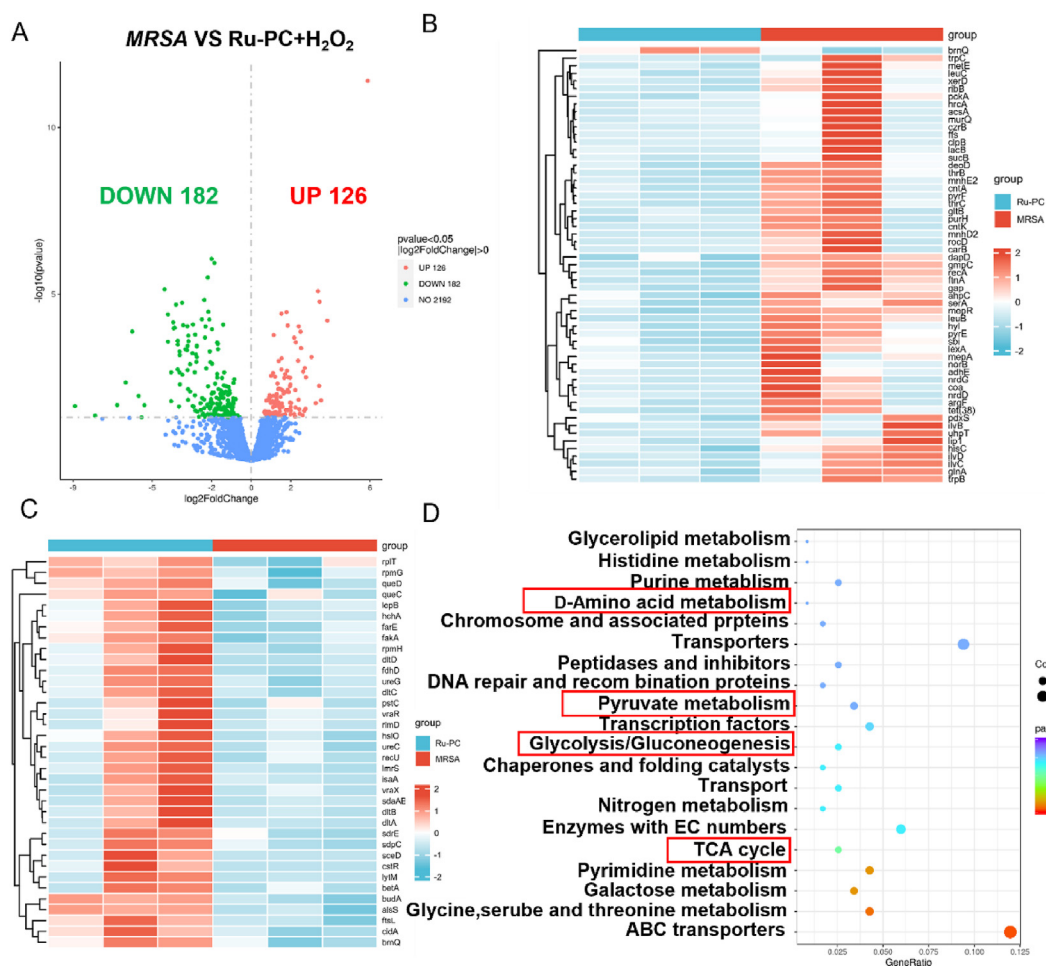
Figure 10 Transcriptomic analysis of MRSA killing by Ru-PC NPs. (A) Volcano map for the distribution of DEGs. Red and green points correspond to 2.0-fold changes in the two groups; (B,C) Hierarchical clustering analysis of the two groups; (D) KEGG enrichment analysis scatter plot.
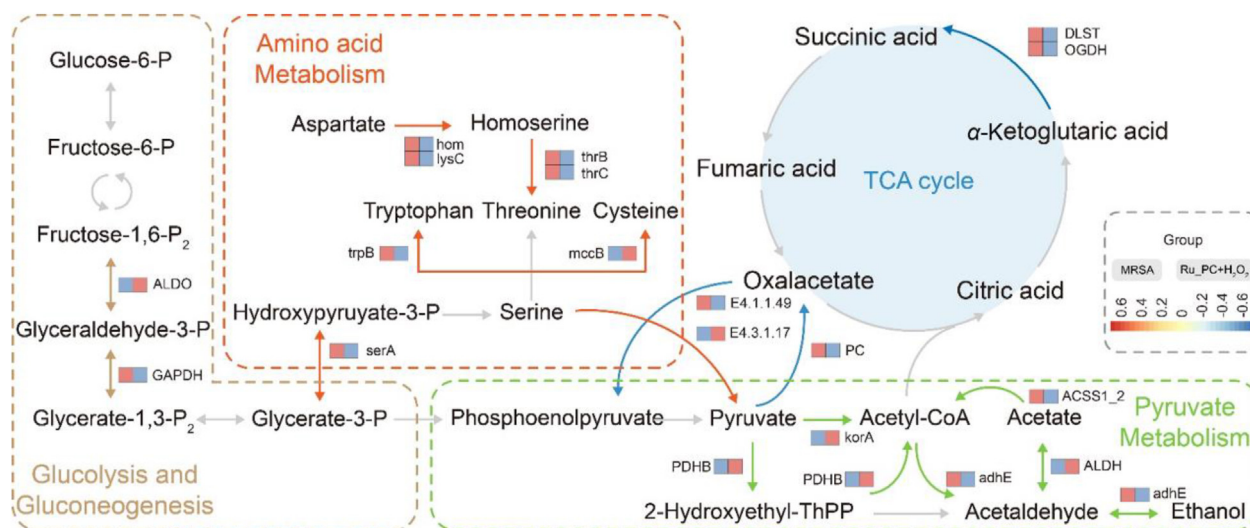
Figure 11 Schematic diagram of the Ru-PC NP bactericidal mechanism in *MRSA*. The glycolysis of bacteria is primarily affected by the bactericidal mechanism of Ru-PC NPs, which interferes with pyruvate metabolism and inhibits the TCA cycle, thereby potentially impacting energy metabolism. Furthermore, the material can influence organismal metabolism by inducing changes in the expression of genes associated with various amino acid metabolic pathways, with a significant upregulation observed in genes related to the regulation of synthetic cysteine.

Second, Ru-PC NPs + H_2O_2 was observed to interfere with pyruvate metabolism and inhibit the TCA cycle, thereby impeding energy metabolism and cell proliferation in bacteria[49]. Pyruvate metabolism is closely related to acid−base homeostasis and redox status; thus, regulating genes related to pyruvate metabolism can impact the bacterial internal environment and lead to bacterial death or apoptosis[50]. Hence, inhibiting the TCA cycle and regulating pyruvate metabolism are crucial for Ru-PC NPs to exert their antibacterial effects.

Finally, Ru-PC NPs were shown to affect bacterial somatic metabolism by altering the expression of genes related to several amino acid metabolic pathways. Upregulation of genes involved in cysteine synthesis was found to enhance the reducing and antioxidant capacity of the organism, thereby improving its antimicrobial activity. Cysteine is a vital antioxidant involved in the detoxification of cells in organisms and serves as an important source of sulfur for the synthesis of other thiosubstitutes, such as thiols and disulfide-bonded proteins[51].

Overall, our findings demonstrate that the bactericidal mechanism of Ru-PC NPs mainly interferes with pyruvate metabolism by inhibiting bacterial glycolysis and suppressing the TCA cycle, thereby modulating energy metabolism. Furthermore, the regulation of gene expression related to amino acid metabolism, especially those involved in cysteine synthesis, is influenced by Ru-PC NPs, which affects the organism's metabolism. As shown in Fig. 11, this study provides new perspectives on the antimicrobial mechanisms of Ru-PC NPs, and their potential as a highly effective antimicrobial agent is emphasized[52].

4. Conclusions

A novel nanozyme, Ru-PC NPs, was developed in this study with quadruple enzymatic activity for treating infected wounds. Strong antimicrobial activity against *E. coli* and *MRSA* was observed for Ru-PC NPs, which was attributed to their POD-like activity, ability to cause GSH loss, and cat-like activity that promoted oxygen replenishment. Remarkable antioxidant capacity was observed in Ru-PC NPs, which allowed them to scavenge surplus ROS and RNS, thereby maintaining the balance of the antioxidant system and preventing inflammation. Additionally, the PC molecules present in Ru-PC NPs exhibited anti-inflammatory properties that inhibited the release of inflammatory factors from macrophages and facilitated their conversion to the M2 phenotype. Furthermore, *in vitro* studies indicated that Ru-PC NPs could stimulate cell proliferation, leading to wound healing by eliminating bacteria, reducing inflammation, providing oxygen, regulating free radical levels, and promoting vascular growth. Ru-PC NPs can inhibit glycolysis in *MRSA* and the TCA cycle, interfere with pyruvate metabolism, and upregulate cysteine synthesis, thus achieving excellent antibacterial effects. These findings underscore the critical role of Ru-PC NPs nanozymes in accelerating the healing of infected wounds, suggesting that multifunctional nanozymes can expedite the wound-healing process.

Author contributions

Jie Shan: Conceptualization, Investigation, Methodology, Writing d original draft. Xu Jin and Cong Zhang: Figure design and review. Mucheng Huang: Figure design and review. Jianghao Xing

Conflicts of interest

Appendix A.   Supporting information

Supporting data to this article can be found online at https://doi.org/10.1016/j.apsb.2023.12.017.

References

1. Wu HY, Chang PH, Chen KY, Lin IF, Hsih WH, Tsai WL, et al. Coronavirus disease 2019 (COVID-19) associated bacterial coinfection: incidence, diagnosis and treatment. *J Microbiol Immunol Infect* 2022;**55**:985−92.

2. Qi X, Xiang Y, Cai E, Ge X, Chen X, Zhang W, et al. Inorganic−organic hybrid nanomaterials for photothermal antibacterial therapy. *Coord Chem Rev* 2023;**496**:215426.

3. He X, Qian Y, Wu C, Feng J, Sun X, Zheng Q, et al. Entropy-mediated high-entropy MXenes nanotherapeutics: NIR-II-enhanced intrinsic oxidase mimic activity to combat methicillin-resistant staphylococcus aureus infection. *Adv Mater* 2023;**35**:e2211432.

4. He X, Hou JT, Sun X, Jangili P, An J, Qian Y, et al. NIR-II photo-amplified sonodynamic therapy using sodium molybdenum bronze nanoplatform against subcutaneous staphylococcus aureus infection. *Adv Funct Mater* 2022;**32**:2203964.

5. Stocker M, Klingenberg C, Navér L, Nordberg V, Berardi A, El Helou S, et al. Less is more: antibiotics at the beginning of life. *Nat Commun* 2023;**14**:2423.

6. Xie M, Gao M, Yun Y, Malmsten M, Rotello VM, Zboril R, et al. Antibacterial nanomaterials: mechanisms, impacts on antimicrobial resistance and design principles. *Angew Chem Int Ed Engl* 2023;**62**: e202217345.

7. Tu J, Liu N, Huang Y, Yang W, Sheng C. Small molecules for combating multidrug-resistant superbug *Candida auris* infections. *Acta Pharm Sin B* 2022;**12**:4056−74.

8. Gow NAR, Johnson C, Berman J, Coste AT, Cuomo CA, Perlin DS, et al. The importance of antimicrobial resistance in medical mycology. *Nat Commun* 2022;**13**:5352.

9. Makabenta JMV, Nabawy A, Li C-H, Schmidt-Malan S, Patel R, Rotello VM. Nanomaterial-based therapeutics for antibiotic-resistant bacterial infections. *Nat Rev Microbiol* 2021;**19**:23−36.

10. Tian H, Yan J, Zhang W, Li H, Jiang S, Qian H, et al. Cu-GA-coordination polymer nanozymes with triple enzymatic activity for wound disinfection and accelerated wound healing. *Acta Biomater* 2023;**167**:449−62.

11. Wang X, Shi Q, Zha Z, Zhu D, Zheng L, Shi L, et al. Copper single-atom catalysts with photothermal performance and enhanced nanozyme activity for bacteria-infected wound therapy. *Bioact Mater* 2021; **6**:4389−401.

12. Ma Y, Jiang K, Chen H, Shi Q, Liu H, Zhong X, et al. Liquid exfoliation of V8C7 nanodots as peroxidase-like nanozymes for photothermal-catalytic synergistic antibacterial treatment. *Acta Biomater* 2022;**149**:359−72.

13. Shen X, Ma R, Huang Y, Chen L, Xu Z, Li D, et al. Nano-decocted ferrous polysulfide coordinates ferroptosis-like death in bacteria for anti-infection therapy. *Nano Today* 2020;**35**:100981.

14. Lyu Z, Ding S, Du D, Qiu K, Liu J, Hayashi K, et al. Recent advances in biomedical applications of 2D nanomaterials with peroxidase-like properties. *Adv Drug Deliv Rev* 2022;**185**:114269.

15. Dong H, Du W, Dong J, Che R, Kong F, Cheng W, et al. Depletable peroxidase-like activity of Fe_3O_4 nanozymes accompanied with separate migration of electrons and iron ions. *Nat Commun* 2022;**13**: 5365.

16. Liu L, Zhang H, Xing S, Zhang Y, Shangguan L, Wei C, et al. Copper-zinc bimetallic single-atom catalysts with localized surface plasmon resonance-enhanced photothermal effect and catalytic activity for melanoma treatment and wound-healing. *Adv Sci* 2023;**10**: e2207342.

17. Liang M, Shang L, Yu Y, Jiang Y, Bai Q, Ma J, et al. Ultrasound activatable microneedles for bilaterally augmented sono-chemodynamic and sonothermal antibacterial therapy. *Acta Biomater* 2023;**158**:811−26.

18. Zhou X, Zhang S, Liu Y, Meng J, Wang M, Sun Y, et al. Antibacterial cascade catalytic glutathione-depleting MOF nanoreactors. *ACS Appl Mater Interfaces* 2022;**14**:11104−15.

19. Wang L, Zhang X, You Z, Yang Z, Guo M, Guo J, et al. A molybdenum disulfide nanozyme with charge-enhanced activity for ultrasound-mediated cascade-catalytic tumor ferroptosis. *Angew Chem Int Ed Engl* 2023;**62**:e202217448.

20. Zhu S, Zhao B, Li M, Wang H, Zhu J, Li Q, et al. Microenvironment responsive nanocomposite hydrogel with NIR photothermal therapy, vascularization and anti-inflammation for diabetic infected wound healing. *Bioact Mater* 2023;**26**:306−20.

21. Shen Y, Nie C, Pan T, Zhang W, Yang H, Ye Y, et al. A multifunctional cascade nanoreactor based on Fe-driven carbon nanozymes for synergistic photothermal/chemodynamic antibacterial therapy. *Acta Biomater* 2023;**168**:580−92.

22. Qiao Y, He J, Chen W, Yu Y, Li W, Du Z, et al. Light-activatable synergistic therapy of drug-resistant bacteria-infected cutaneous chronic wounds and nonhealing keratitis by cupriferous hollow nanoshells. *ACS Nano* 2020;**14**:3299−315.

23. Gao W, Zhang L. Nanomaterials arising amid antibiotic resistance. *Nat Rev Microbiol* 2021;**19**:5−6.

24. Han Z, Gao X, Wang Y, Cheng S, Zhong X, Xu Y, et al. Ultrasmall iron-quercetin metal natural product nanocomplex with antioxidant and macrophage regulation in rheumatoid arthritis. *Acta Pharm Sin B* 2023;**13**:1726−39.

25. Qu X, Gao C, Fu L, Chu Y, Wang J-H, Qiu H, et al. Positively charged carbon dots with antibacterial and antioxidant dual activities for promoting infected wound healing. *ACS Appl Mater Interfaces* 2023;**15**: 18608−19.

26. Ye L, Fan S, Zhao P, Wu C, Liu M, Hu S, et al. Potential herb−drug interactions between anti-COVID-19 drugs and traditional Chinese medicine. *Acta Pharm Sin B* 2023;**13**:3598−637.

27. Dong S, Guo X, Han F, He Z, Wang Y. Emerging role of natural products in cancer immunotherapy. *Acta Pharm Sin B* 2022;**12**: 1163−85.

28. Ye J, Li Q, Zhang Y, Su Q, Feng Z, Huang P, et al. ROS scavenging and immunoregulative EGCG@Cerium complex loaded in antibacterial polyethylene glycol-chitosan hydrogel dressing for skin wound healing. *Acta Biomater* 2023;**166**:155−66.

29. Sun B, Wang X, Ye Z, Zhang J, Chen X, Zhou N, et al. Designing single-atom active Sites on sp2 -carbon linked covalent organic frameworks to induce bacterial ferroptosis-like for robust anti-infection therapy. *Adv Sci* 2023;**10**:e2207507.

30. Liu K, Zhang C, Chang R, He Y, Guan F, Yao M. Ultra-stretchable, tissue-adhesive, shape-adaptive, self-healing, on-demand removable hydrogel dressings with multiple functions for infected wound healing in regions of high mobility. *Acta Biomater* 2023;**166**: 224−40.

31. Yuan R, Li Y, Han S, Chen X, Chen J, He J, et al. Fe-curcumin nanozyme-mediated reactive oxygen species scavenging and anti-inflammation for acute lung injury. *ACS Cent Sci* 2022;**8**:10−21.

32. Zhang R, Cheng L, Dong Z, Hou L, Zhang S, Meng Z, et al. Ultra-small natural product based coordination polymer nanodots for acute kidney injury relief. *Mater Horiz* 2021;**8**:1314−22.

33. Liu Y, Li C, Tan C, Pei Z, Yang T, Zhang S, et al. Electrosynthesis of chlorine from seawater-like solution through single-atom catalysts. *Nat Commun* 2023;**14**:2475.

34. Feng D, Wang P, Qin R, Shi W, Gong L, Zhu J, et al. Flower-like amorphous MoO$_{3-x}$ stabilized Ru single atoms for efficient overall water/seawater splitting. *Adv Sci* 2023;**10**:e2300342.

35. Fan H, Zheng J, Xie J, Liu J, Gao X, Yan X, et al. Surface ligand engineering ruthenium nanozyme superior to horseradish peroxidase for enhanced immunoassay. *Adv Mater* 2023:e2300387.

36. Hu B, Xiao X, Chen P, Qian J, Yuan G, Ye Y, et al. Enhancing anti-tumor effect of ultrasensitive bimetallic RuCu nanoparticles as radiosensitizers with dual enzyme-like activities. *Biomaterials* 2022;**290**: 121811.

37. Yi J, Deng Q, Liu Z, Wang H, Liu X, Ren J, et al. Nanozyme-based supramolecular self-assembly as an artificial host defense system for treatment of bacterial infections. *Small* 2023;**19**:e2301096.

38. Jin X, Zhang W, Shan J, He J, Qian H, Chen X, et al. Thermosensitive hydrogel loaded with nickel-copper bimetallic hollow nanospheres with SOD and CAT enzymatic-like activity promotes acute wound healing. *ACS Appl Mater Interfaces* 2022;**14**:50677−91.

39. Tian X, Wang P, Li T, Huang X, Guo W, Yang Y, et al. Self-assembled natural phytochemicals for synergistically antibacterial application from the enlightenment of traditional Chinese medicine combination. *Acta Pharm Sin B* 2020;**10**:1784−95.

40. Zhao X, Feng J, Zhang J, Han Z, Hu Y, Shao H-H, et al. Discovery and druggability evaluation of pyrrolamide-type GyrB/ParE inhibitor against drug-resistant bacterial infection. *Acta Pharm Sin B* 2023;**13**: 4945−62.

41. Zhou W, Duan Z, Zhao J, Fu R, Zhu C, Fan D. Glucose and MMP-9 dual-responsive hydrogel with temperature sensitive self-adaptive shape and controlled drug release accelerates diabetic wound healing. *Bioact Mater* 2022;**17**:1−17.

42. Chen Y, Wu G, Li M, Hesse M, Ma Y, Chen W, et al. LDHA-mediated metabolic reprogramming promoted cardiomyocyte proliferation by alleviating ROS and inducing M2 macrophage polarization. *Redox Biol* 2022;**56**:102446.

43. Xu Z, Qiu Z, Liu Q, Huang Y, Li D, Shen X, et al. Converting organosulfur compounds to inorganic polysulfides against resistant bacterial infections. *Nat Commun* 2018;**9**:3713.

44. Liu Y, Zhuang B, Yuan B, Zhang H, Li J, Wang W, et al. Predatory bacterial hydrogels for topical treatment of infected wounds. *Acta Pharm Sin B* 2023;**13**:315−26.

45. Li Y, Fu R, Duan Z, Zhu C, Fan D. Artificial nonenzymatic antioxidant mXene nanosheet-anchored injectable hydrogel as a mild photothermal-controlled oxygen release platform for diabetic wound healing. *ACS Nano* 2022;**16**:7486−502.

46. Bai Q, Zheng C, Sun N, Chen W, Gao Q, Liu J, et al. Oxygen-releasing hydrogels promote burn healing under hypoxic conditions. *Acta Biomater* 2022;**154**:231−43.

47. Jariwala N, Ozols M, Bell M, Bradley E, Gilmore A, Debelle L, et al. Matrikines as mediators of tissue remodelling. *Adv Drug Deliv Rev* 2022;**185**:114240.

48. Yazarlu O, Iranshahi M, Kashani HRK, Reshadat S, Habtemariam S, Iranshahy M, et al. Perspective on the application of medicinal plants and natural products in wound healing: a mechanistic review. *Pharmacol Res* 2021;**174**:105841.

49. He J, Zhang Y, Yu X, Xu C. Wearable patches for transdermal drug delivery. *Acta Pharm Sin B* 2023;**13**:2298−309.

50. Toller-Kawahisa JE, O'Neill LAJ. How neutrophil metabolism affects bacterial killing. *Open Biol* 2022;**12**:220248.

51. Shu X, Shi Y, Huang Y, Yu D, Sun B. Transcription tuned by *S*-nitrosylation underlies a mechanism for *Staphylococcus aureus* to circumvent vancomycin killing. *Nat Commun* 2023;**14**:2318.

52. Allen JE. IL-4 and IL-13: regulators and effectors of wound repair. *Annu Rev Immunol* 2023;**41**:229−54.